S & M 4164

Slope-adaptive Elliptical Neighborhood Algorithm for Denoising Photon-counting LiDAR Data in Complex Terrain

Kuifeng Luan,^{1,2} Lizhe Zhang,^{1*} Weidong Zhu,^{1,2} Wei Kong,³ Lin Liu,¹ Jinhui Zheng,¹ Peiyao Zhang,¹ Xiangrong Chen,¹ and Hui Jiang¹

¹Shanghai Ocean University, No. 999 Hucheng Ring Road, Lingang New City, Shanghai 201306, China ²Estuarine and Oceanographic Mapping Engineering Research Center of Shanghai, No. 999 Hucheng Ring Road, Lingang New City, Shanghai 201306, China ³Key Laboratory of Space Active Optical-Electro Technology Shanghai Institute of Technical Physics Chinese Academy of Sciences, No. 500 Yutian Road, Hongkou District, Shanghai 200083, China

(Received April 14, 2025; accepted August 28, 2025)

Keywords: ICESat-2 photon data, adaptive elliptical neighborhood, local terrain features, denoising, complex terrain

The Ice, Cloud, and Land Elevation Satellite-2 (ICESat-2), owing to its sensitive photon detection system, acquires data containing a large number of background noise photons, which seriously affects the accuracy of signal extraction in complex terrain regions. To address the problem of insufficient parameter adaptability in existing denoising algorithms for slope-varying regions, we propose a denoising algorithm for slope-adaptive elliptic neighborhoods (SAEN-D), which is based on local terrain features. First, the effective signal range is intercepted by histogram statistics, and more than 88.82% of the discrete noise is preprocessed and rejected using grid statistics. Then, an adaptive elliptic neighborhood with slope angle constraints is constructed by a slope-driven segmentation strategy, and the search direction and the length of the ellipse's long-axis are dynamically adjusted to match the signal distribution characteristics. Finally, the combination of the local distance discrepancy coefficient and OTSU's method (OTSU) of thresholding segmentation is used to accurately distinguish signal and noise photons. Experiments are carried out in the regions of Antarctica's flat ice cap and Greenland's complex terrain, and the results show that in extreme terrains such as that with steep slopes and elevation faults, the value of the method described in this paper reaches 96.13–98.25%, which is 7.8% higher than that of the traditional improved local sparse coefficient (ILSC) algorithm. The results of the study confirm that SAEN-D effectively solves the problem of signal leakage and misjudgment caused by the anisotropy of photon distribution in complex terrain, and provides reliable support for high-precision elevation inversion and the dynamic monitoring of ICESat-2 data. This algorithm has broad application potential, as it can significantly improve the quality of laser altimetry satellite data and offers new insights and solutions for precise monitoring using sensor technologies in complex and variable terrains.

^{*}Corresponding author: e-mail: <u>m220200695@st.shou.edu.cn</u> https://doi.org/10.18494/SAM5693

1. Introduction

In the context of global climate change, monitoring the mass balance of polar ice caps is one of the core tasks in assessing the risk of sea-level rise. Traditional optical and radar remote sensing techniques are limited by either insufficient spatial resolution or penetration capability, making it challenging to accurately detect millimeter-scale elevation changes on ice sheet surfaces. The National Aeronautics and Space Administration (NASA) launched the Ice, Cloud, and Land Elevation Satellite-2 (ICESat-2) with the Advanced Terrain Laser Altimeter System (ATLAS), which, for the first time, used single-photon counting technology to emit laser pulses at a repetition rate of 10 kHz, realizing submeter spatial resolution and centimeter-level elevation accuracy. (1-3) This technological breakthrough has established ICESat-2 as a pivotal instrument for high-precision monitoring across diverse domains, such as polar ice caps, forest canopies, and shallow ocean topography. (4) However, the single-photon detection mechanism introduces significant technical challenges while improving sensitivity: interference from solar background noise, atmospheric scattering, and multiple reflections from the surface result in data containing a large number of background noise photons, (5) especially in complex terrain regions with steep slopes and broken surfaces, where the spatial distributions of the noise and signal photons are highly overlapping, severely constraining the data usability. (6) Therefore, the study of adaptive photon denoising algorithms is a key prerequisite for the conversion of ICESat-2 data from raw photon clouds to reliable surface elevation information. (7,8)

In recent years, denoising methods for photon point clouds have primarily fallen into three categories: rasterization processing, density clustering, and local statistical parameters. (4) Some scholars rasterize the photon point cloud dataset by taking the number of photons in the grid as the pixel value and adopting image processing techniques to eliminate noise points, but the process of rasterization inevitably loses the details of the spatial distribution of the photons, which results in the over-smoothing of tiny topographic features, and does not guarantee the accuracy of the denoising algorithm. (9-12) The density clustering method is based on the assumption of the spatial aggregation of signal photons and utilizes a density clustering model to distinguish noise. For example, Zhang and Kerekes proposed an improved density-based spatial clustering of applications with noise (DBSCAN), which improves the denoising accuracy under flat terrain conditions. (13) In addition, Zhu et al. (3) proposed the ordering points to identify the clustering structure (OPTICS) algorithm based on the ordering of points to adapt to the multiscale density distribution through core distance optimization as a way to accomplish the denoising task. However, such methods face two major bottlenecks in complex terrain: (i) the fixed shape of the search window is difficult to match with the anisotropic photon distribution caused by the slope, and the signals are highly susceptible to missed detection in steep slope regions; (ii) the density threshold relies on empirical settings and lacks a dynamic response to localized terrain features. (14) The third category of methods, local distance statistics methods, involves constructing adaptive thresholds by analyzing the local statistical properties (e.g., distance and density differences) of photon distributions. The differential regressive and Gaussian adaptive nearest neighbor (DRAGANN) algorithm was proposed by Neuenschwander and Pitts⁽¹⁵⁾ and adopted by NASA as a standard denoising tool for the extraction of signal

photons from ICESat-2's ATL03 data to extract signal photons and ultimately generate the ATL08 data product. Herzfeld *et al.* used spatial statistics and discrete mathematical concepts to distinguish between noise and signal photons in ICESat-2 data, using parameters such as radial basis functions, density metrics, geometric anisotropy, and eigenvectors, and accomplished high-precision observations of complex terrain with crevassed ice. (16) Chen *et al.* proposed an ellipsoidal density-based local outlier factor (LOF) detection algorithm to quantify photon outliers by calculating the local density difference between each data point and its neighbors (local neighborhood statistical properties), which, although it performs well in vegetated regions, fails to address the blurring of the boundary of the signal-to-noise distribution in ice-cap terrain. (17) Xie *et al.* proposed a density-based adaptive method (DBAM) to enhance the adaptability of complex terrain through elliptical direction optimization and OTSU threshold segmentation, but there is no reference value for its elliptical direction, and it still requires several iterations to adjust the parameters in steep slope regions, which makes the computational efficiency low. (1)

In summary, the existing methods for denoising in complex terrain suffer from fragmented adaptation mechanisms in the direction and size of the ellipse, the lack of coordinated response to terrain variations, and reliance on manual parameter tuning, all of which limit their scalability for large-scale data applications. To address these issues, we propose a photon data denoising algorithm based on local terrain features, termed slope-adaptive elliptic neighborhoods denoising (SAEN-D). This algorithm constructs direction- and size-adaptive elliptic neighborhoods and establishes a dual adaptive mechanism for terrain-slope coupling by dynamically associating the elliptic direction and slope angle; proposes a dynamic segmentation and merging strategy based on the idea of dividing slope consistency intervals by cubic spline interpolation and curvature detection; and computes the local distance statistical parameter and dynamic segmentation threshold by the OTSU method. The three innovations work synergistically to address challenges in complex terrain, such as the insufficient self-adaptation of ellipse shape, computational redundancy, and limitations of global assumptions, thereby providing a systematic solution for denoising ICESat-2 photon data. The denoising method proposed in this paper not only significantly improves the data processing accuracy and stability of laser altimetry sensors in complex terrain environments, but also provides strong support for the in-depth application of sensor technologies in fine-scale terrain perception systems.

2. Data and Methods

2.1 Research data and preprocessing

2.1.1 Research data

To verify the effectiveness of the algorithm in complex terrain regions, we select ICESat-2 data from two typical land ice regions for experimental validation. The ATL03 data belongs to the ICESat-2 data's level 2A data product, which contains the global geolocation of the photon data, and the photon events recorded by ATLAS are expressed in terms of latitude, longitude,

time of arrival, and ellipsoidal altitude. The photon profile information can be obtained by reading the ATL03 data. As shown in Fig. 1(a), DATA_1, with the data name ATL03_201810212 00424_03540110_006_02.h5, used in this study is the ATL03 data transiting Northeast Antarctica on October 21, 2018, as shown in Fig. 1(b), and intercepts the land-ice region within 400–402 s of the gtlr beam, within the study area with little overall undulation and gentle slopes. DATA_2, with the data name ATL03_20181109172947_06430103_006_02.h5, is the ATL03 data transiting Southwest Greenland on November 09, 2018, as shown in Fig. 1(c), and intercepts the land-ice region within 202–204 s of the gtlr beam; this region has a considerable topographic fluctuation and a steep slope and includes a section of the sea surface.

The photon point cloud profiles intercepted in the two regions are shown in Fig. 2, and the horizontal and vertical coordinates are the along-track distance and photon elevation, respectively. Figure 2(a) shows the land-ice sheet region in Northeast Antarctica, with gentle terrain changes, a maximum elevation difference of about 10 m, high data continuity in the

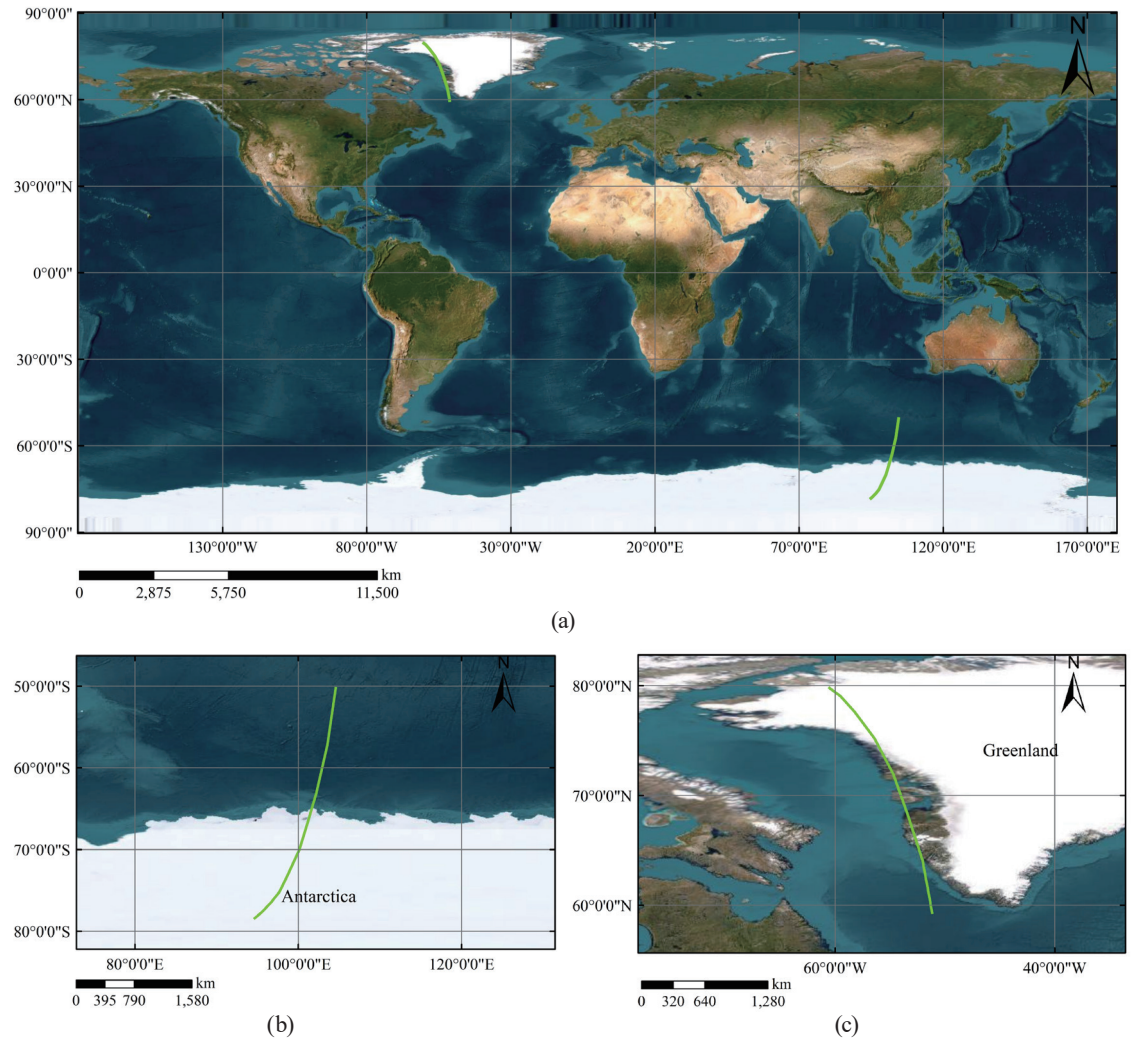


Fig. 1. (Color online) (a) Experimental regional dataset acquisition trajectory, (b) Antarctic regional dataset, and (c) Greenland regional dataset.

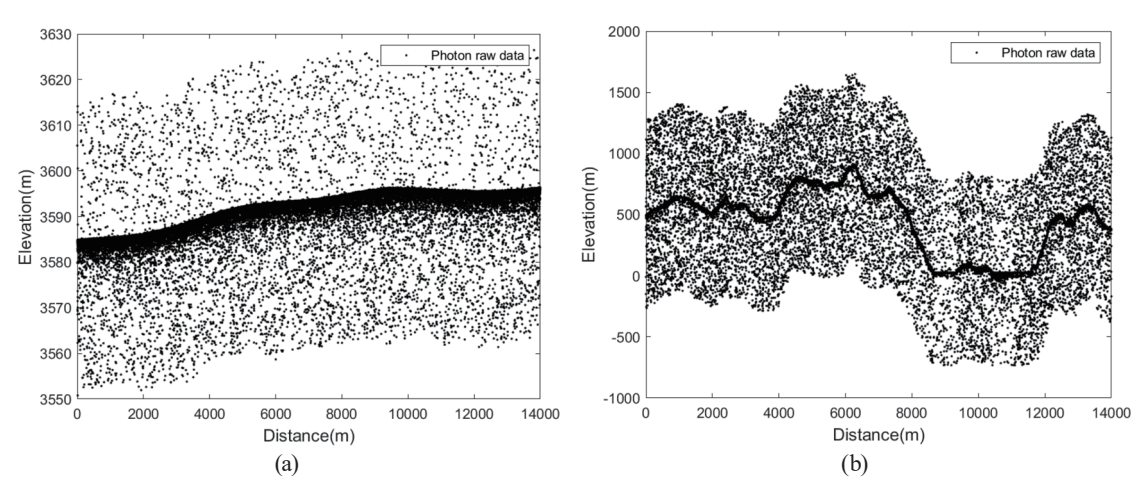


Fig. 2. Raw point cloud data for the land-ice regions of (a) Northeast Antarctica and (b) Southwest Greenland.

elevation direction, and signal photons densely distributed near the surface of the land-ice sheet, with discrete random noise distributed around the surface. The closer to the surface, the higher the density of the point cloud. Figure 2(b) shows the land-ice sheet area in southwest Greenland. This region has complex topography, large undulations, and a maximum elevation difference of about 950 m. In the steep area, owing to the drastic slope change, the photon point cloud is relatively sparse in some areas, and there is data discontinuity in the elevation direction.

2.1.2 Photon preprocessing

The photon data contains a large number of noise photons that are closely related to the external environment and are discretely and randomly distributed, and there is also a great difference in the spatial distribution of noise and signal photons, with the signal photons being more tightly distributed than the noise photons. On this basis, we can preprocess the photon dataset, which mainly includes the interception of the effective signal range of the photons and the preliminary denoising process based on grid statistics, with the main purpose of removing unnecessary noise photons and locating a more accurate region for the subsequent photon data processing.⁽¹⁸⁾

By analyzing the characteristics of photon data, we find that the spatial distribution location of signal photons is more concentrated, and the effective range of the signal in the direction of the longitudinal axis is smaller. To reduce unnecessary calculations, the effective signal range of photon data can be intercepted before the initial denoising. In this study, we mainly use the method of histogram statistics to construct the histogram in the direction of the slant distance of the longitudinal axis, count the number of photons in each data segment, and use the threshold to intercept the effective signal range.

Because of the random distribution of noise throughout the grid space, cells with a large number of photons can indicate the presence of signal photons. In this study, a coarse denoising method based on grid statistics is used to divide the distance and elevation along the track into equal distances, and the grid cells with the maximum total number of photons in each grid along the track distance × elevation are recognized as possible signal cells.

2.2 General description of the experimental procedure

After preprocessing, there is still a large amount of noise near the surface data. To take into account the impact of local terrain features on the photon signal distribution, and to retain the local effective terrain features, in this study, the data are segmented, the direction of the long axis of the elliptic neighborhood is adaptively changed in accordance with the direction of the slope, and the shape and size of the neighborhood can be adjusted in accordance with the terrain features, combined with experience. Then, a local threshold is used to detect the ground signal photons to minimize the effect of the variation of terrain along the track on the signal distribution. After the above three processes, the technical framework of the photon data denoising method based on local terrain features to create direction- and size-adaptive elliptic neighborhoods is constructed. The specific flow is shown in Fig. 3.

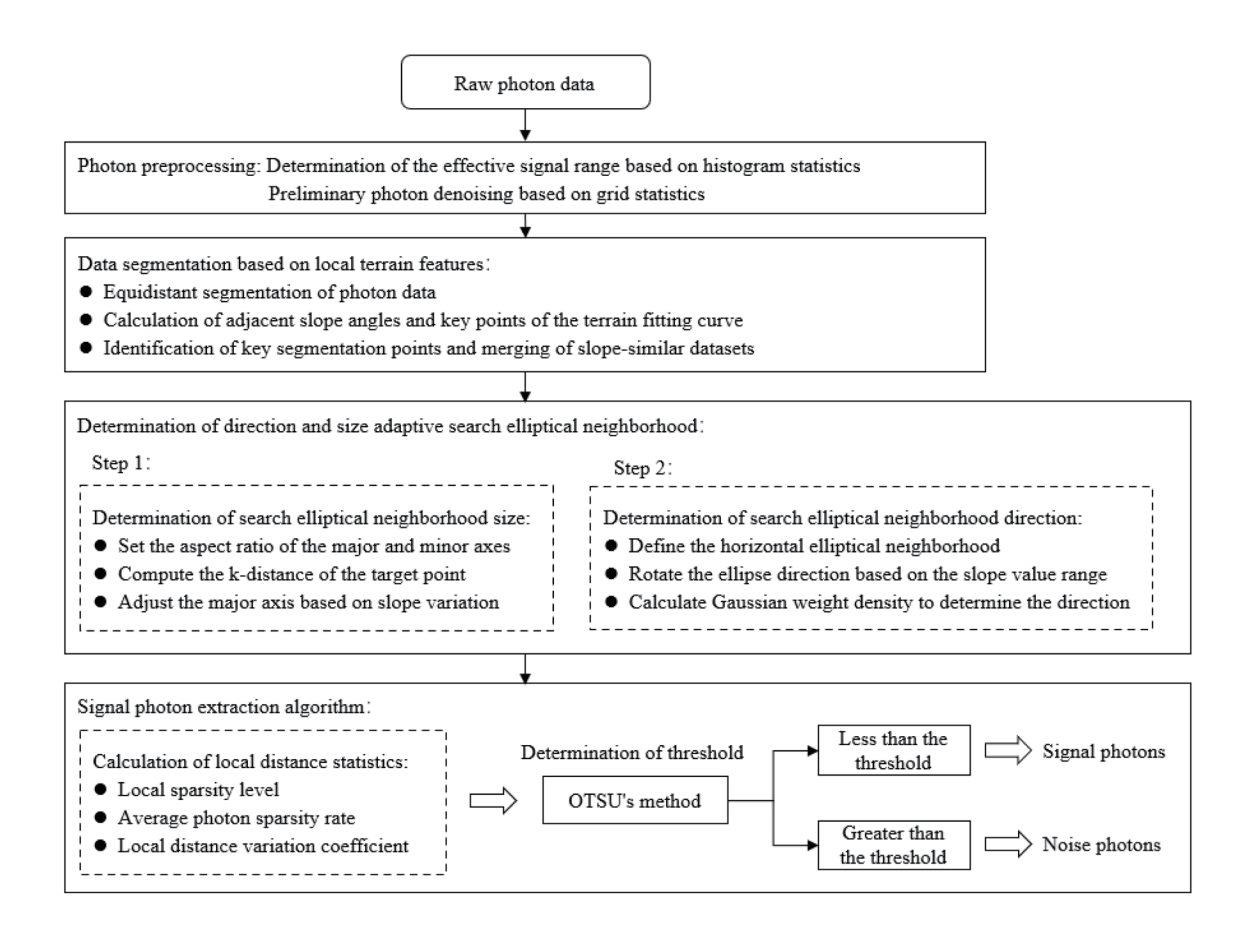


Fig. 3. Flowchart of the proposed SAEN-D technology.

2.3 Data segmentation and merging based on local topographic features

2.3.1 Equidistant segmentation of data along the track direction

The preprocessed data are divided into small segments at equal intervals along the track direction. The segmentation distance is determined on the basis of the along-track length of the extracted data and the point cloud density. In general, overly short segments may ignore the spatial distribution of surrounding points, limiting the algorithm's ability to account for local terrain features. On the other hand, overly long segments, especially when processing dense point clouds over extended distances, can lead to memory overload and computational inefficiency. Therefore, the segmentation distance must ensure a moderate number of points per segment while preserving local terrain characteristics. Referring to the results of tests conducted on the selected study areas, the segment length—also referred to as the Δl size—is set to 20 m, and the segmented dataset $L = \{L_1, L_2, L_3, ..., L_n\}$ is constructed, where n is the number of segmented datasets, and the photon data that fall into each segmented dataset are counted and given labels.⁽¹⁹⁾

$$l_k = k \cdot \Delta l, \ k = 0, 1, 2, ..., n - 1$$
 (1)

k is the index of the segment to which the photon belongs, $\Delta l = 20$ m is the length of the segment, and the photon point falls into segment L_{k+1} when the photon point is at distance $l \in [l_k, l_{k+1}]$ along the track.

To be representative of the topographic features within the segmented dataset, we calculated the maximum density of points, where the concept of elliptical neighborhood density was used to measure the local denseness of each point. First, for each point, we calculate its elliptical distance from other points in the group d_{mn} , and then count the number of points within the ellipse and accumulate the density ρ_m . By comparing the density of each point, we determine the point with the highest density and record its serial number to construct the maximum density point dataset I.

$$d_{mn} = \sqrt{\left(\frac{x_m - x_n}{a_0}\right)^2 + \left(\frac{y_m - y_n}{b_0}\right)^2}$$
 (2)

$$\rho_m = \sum_{m=1}^{N} K(d_{mn}) \tag{3}$$

 (x_m, y_m) represents the center point of the current search ellipse. Since it is necessary to calculate the elliptical neighborhood for each photon in the dataset, the value of (x_m, y_m) spans all photon points within the dataset. a_0 and b_0 denote the lengths of the semi-major and semi-minor axes of the ellipse, respectively. (x_n, y_n) refers to the coordinates of other points within the segmented

dataset, which are used to compute the coordinate distance from the current search ellipse center point to these points. When $d_{mn} \leq 1$ is considered, point n is regarded as being within the elliptical neighborhood centered at point m, and the coordinates of $K(d_{mn}) = 1$ are recorded. N represents the total number of photon points in the entire dataset. ρ_m denotes the cumulative density value of all points within the elliptical neighborhood centered at point m.

Slope angle is an important basis for judging the trend of terrain change, and it can be used to analyze the local trend of the point cloud and to calculate the adjacent slope angle by calculating the lateral and vertical differences of the adjacent maximum density points. The specific equations are as follows.

$$\begin{cases} slope_{dx(i)} = x(i) - x(i-1) \\ slope_{dy(i)} = y(i) - y(i-1) \\ \theta_i = \arctan_2 \left(slope_{dy(i)}, slope_{dx(i)} \right) \end{cases}$$
 (4)

 $slope_{dx(i)}$ is the horizontal difference between neighboring maximum density points, $slope_{dy(i)}$ is the vertical difference, i is the index of the maximum density point, x(i) and y(i) represent its horizontal and vertical coordinates, respectively, and $arctan_2(slope_{dx(i)}, slope_{dy(i)})$ denotes the two-argument arctangent function. Using these parameters, the adjacent slope angle of the photon data, θ_i , is computed. The neighboring maximum density points are used as the boundary, and the slope is assigned to all photon points that fall within the interval.

2.3.2 Merging of slope similarity datasets

A. Curve fitting and detection of critical points

Combined with the local terrain features, we use the cubic spline interpolation method to fit the maximum density points for terrain trend analysis. To capture the trend of the terrain in time, the first-order derivatives of the fitted curves are calculated to obtain the slopes of the neighboring datasets, as shown in Eq. (5), and at the same time, we detect the locations where the derivatives change from positive to negative or from negative to positive and where the bending direction of the curves changes to judge the possible extreme value and inflection points and construct the key point dataset J.

$$\begin{cases} f(x) = \sum_{k=0}^{n} a_k x^k \\ f'(x) = \sum_{k=1}^{n} k \cdot a_k x^{k-1} \end{cases}$$
 (5)

f(x) is the equation of the fitted curve, which represents the continuous variation of the photon data elevation in the direction of the track, x represents the distance of the photon in the direction

of the track, n is the order of the fitted polynomial, and a_k is the coefficient of the polynomial. f'(x) is the first-order derivative of the fitted curve, which represents the rate of change (slope) of the fitted curve at the point, $k \cdot a_k$ is the coefficient of each term of the derivative, and the order in x^{k-1} is the result of subtracting k-1 from k.

B. Key point segmentation

The longitudinal difference, also known as the first-order difference, indicates the magnitude of change between two key points, and the falloff between two key points needs to be considered when segmenting a dataset; the larger the first-order difference, the larger the falloff between two key points and the more likely the key point will be recognized as a segmentation point. The second-order difference can help to find the location with the most significant slope change, which can assist in recognizing terrain inflection points or segmenting terrain area data. The second-order difference variable is calculated from the elevation differences of a key point with its preceding and succeeding neighboring datasets, reflecting local curvature variation, with larger values indicating more pronounced changes; the larger the difference, the more dramatic the change near the point. Use Eq. (6) to calculate the first- and second-order differential variations:

$$\begin{cases} y_{change1(j)} = |y(j) - y(j-1)| \\ y_{change2(j)} = |y(j+1) - 2y(j) + y(j-1)| \end{cases}$$
 (6)

where j is the serial number of the key point, $y(j) \in J$, $y_{changel}(j)$ is the first-order differential variation of the photon data, and $y_{change2}(j)$ is the second-order differential variation of the photon data. To determine whether segmentation is needed, first- and second-order differential values are calculated and compared with predefined thresholds. Setting appropriate thresholds is critical, as it directly affects segmentation accuracy. An overly low threshold may lead to excessive segmentation by capturing minor elevation fluctuations, which leads to misclassifying continuous regions as separate segments. Conversely, a high threshold may cause undersegmentation as subtle terrain changes may be overlooked and key inflection points may not be captured, thus reducing precision. By analyzing the distribution of first- and second-order differences within the point cloud data, a reasonable threshold range is established. Multiple experiments are conducted using a combination of bisection and trial-and-error methods to assess the stability and accuracy of segmentation under different threshold pairs. The final thresholds are set as $thr_1 = 0.5$ m and $thr_2 = 0.1$ m.

C. Merging of datasets

The data segmentation points are identified by determining the key points of terrain changes. Data segments with approximately the same trend are merged in the same data segment, and the slope angles of all photon points of the data segments are merged while merging the small data segments to generate a slope angle dataset, which is defined as $E = \{\theta_1, \theta_2, \theta_3, ..., \theta_n\}$, as the number of small data segments in the merged dataset and the slope angles of the data photon points of the segment are limited to the above slope angle dataset.

2.4 Orientation and size adaptive elliptic neighborhood construction

2.4.1 Search ellipse size adaptation

In the segmented dataset, calculate the Euclidean distance from the point p to be detected to all other object points q in the dataset, and sort the object points q in accordance with the distance. Select the kth distance of point p to determine the size of the search elliptic neighborhood and so on for each photon point in the dataset to construct the corresponding search elliptic neighborhood. k is determined by the trial-and-error method. In this study, k is taken to be 9, that is, the object point q, $k_d(p, q)$ is selected as the kth distance of the point p to be measured, combined with the ratio of the long and short semi-axes to construct the kth distance of the point p to be measured searching for the ellipse neighborhood $D_k(p)$. The curvature of the ellipse plays a critical role in distinguishing between signal and noise photons. A small curvature may result in confusion between the two, while an excessively large curvature may lead to oversegmentation and the loss of valuable signals. The lengths of the major and minor axes of the search ellipse in the horizontal direction are determined empirically. For each selected curvature value, segmentation experiments are conducted to compare the effects of different curvature settings. On the basis of the actual dataset, the spatial aggregation and distribution patterns of visually interpreted signal and noise photons are analyzed. When the number of signal photons is equal in the along-track and elevation directions, the spatial distance ratio between them is calculated and then used to determine the initial aspect ratio of the ellipse, denoted as a:b=5:1.

The terrain in the study area is undulating, when the direction of the long axis of the search ellipse presents a certain angle with the horizontal direction (slope angle), the distance covered by the search ellipse neighborhood in the along-track direction will be reduced, and the size of the long axis, if chosen to be fixed, will result in fewer neighboring photons, and the final density calculation results will be smaller. To ensure the consistency of the search ellipse neighborhood in the horizontal direction, the size of the half-length axis of the search ellipse can be set to vary in accordance with the slope. The larger the slope, the longer the long half-axis of the search ellipse, and the length of the short half-axis is sufficient to ensure that it can cover the range of ground photons. It can be determined that the long semi-axis of the ellipse in the region with slope θ is

$$a' = \frac{a}{\cos \theta},\tag{7}$$

where θ represents the slope of the terrain, a represents the length of the long semi-axis of the ellipse search neighborhood when the laser is illuminated on horizontal terrain, and a' represents the length of the long semi-axis on locally undulating terrain.

2.4.2 Directionally adaptive ellipses based on slope calculations

A. Defining the horizontal ellipse neighborhood

The slope-based calculation of the adaptive search ellipse is defined by taking each photon as the center of an ellipse and determining the direction of the ellipse based on terrain features and ground reflectivity. Before the direction of the ellipse neighborhood becomes adaptive, it is first necessary to define the horizontal search ellipse neighborhood and calculate the distance between the long and short axes of the search ellipse in the horizontal direction, as described in Sect. 2.4.1. Taking point $p(x_p, h_p)$ as the center of the ellipse, its ellipse distance to point $p(x_q, h_q)$ is described by Eq. (8), and it can be determined whether or not point q is in the horizontal search ellipse centered at point p.

$$dist(p,q) = \sqrt{\frac{\Delta X_{\theta}^{2}}{\left(a'\right)^{2}} + \frac{\Delta H_{\theta}^{2}}{\left(b\right)^{2}}}$$
(8)

$$\begin{cases} \Delta X_{\theta} = x_p - x_q \\ \Delta H_{\theta} = h_p - h_q \end{cases}, \ \theta = 0$$
 (9)

Here, a' and b represent the radii of the long and short axes of the ellipse, respectively; ΔX_{θ} represents the horizontal distance difference between p and q in the along-track direction under the condition $\theta = 0$; and ΔH_{θ} represents the height difference between p and q in the elevation direction. When dist(p, q) is less than 1, point q is within the neighborhood of the search ellipse of p. Otherwise, it is outside the neighborhood of the search ellipse.

B. Correction of ellipse neighborhood orientation with reference to slope

The orientation angle of the elliptical neighborhood for each point needs to be determined by continuously rotating the elliptical window. During the rotation process, the number of photons within the elliptical neighborhood is calculated at each angle, using a step size of 5° . By gradually comparing the results across 36 different angles, the direction with the maximum number of photons and the corresponding maximum photon count can be identified. This process involves relatively high computational complexity. In this study, the original dataset is segmented on the basis of the local terrain slope. For each large segment of data, the slope dataset corresponding to each photon point is read. The slope angle of each photon point is constrained within the range defined by the slope angle dataset, which provides a reference for the rough estimation of the slope angle and guides the selection of a suitable range of the orientation angle θ . By adjusting the angle of the major axis of the ellipse, the elliptical neighborhood orientation is determined. The elliptical distance calculation equation is as follows.⁽²⁰⁾

$$\begin{cases} \Delta X_{\theta} = \cos \theta \left(x_p - x_q \right) + \sin \theta \left(h_p - h_q \right) \\ \Delta H_{\theta} = \cos \theta \left(h_p - h_q \right) - \sin \theta \left(x_p - x_q \right) \end{cases}, \quad \theta \in [\min(E), \max(E)] \end{cases}$$
(10)

 ΔX_{θ} and ΔH_{θ} represent the horizontal major-axis distance and vertical minor-axis elevation differences of the rotated elliptical neighborhood, respectively. Dataset E contains all slope angles, where the minimum slope angle is assigned as the initial value of θ . The angle θ is subsequently increased in increments of 5°, and at each increment, the photon density within the corresponding elliptical neighborhood is computed. This iterative process continues until θ reaches the maximum slope angle in dataset E, at which point the incrementation is terminated. Finally, the direction of θ is defined as the angle associated with the maximum photon density among all evaluated orientations.

The distance between the point to be measured and other photon points needs to be taken into account when calculating the photon density in the search elliptic neighborhood, and the density is calculated in a weighted form, with the closer points contributing more. In this paper, the Gaussian kernel method is used to give the weight of each point in the elliptical search region.⁽¹⁾ The weight and density of each photon are calculated using Eq. (11). The sum of the weights of all photons in the elliptical region is defined as the density of the center point of the ellipse.

$$\begin{cases} W_p = \frac{1}{\sqrt{2\pi\sigma^2}} e^{-\left(\frac{dist(p,q)-u}{\sqrt{2}\sigma}\right)^2} \\ \rho_p = \sum_{x \in D_k(p)} W_p \end{cases}$$
(11)

Here, u represents the mean of the Gaussian function and is set to 0; σ represents the variance of the Gaussian function; W_p represents the weight of each photon in the elliptical search region of p; $D_k(p)$ represents the elliptical search area; and ρ_p represents the density of p. To determine the accurate direction of the maximum weighted density (with a θ error not exceeding 1°), the weighted photon density within each search elliptical neighborhood is calculated for different slope angles, at 1° intervals, within the range of $\theta \pm 5$ °. The direction corresponding to the maximum photon density is taken as the precise major axis direction of the search elliptical neighborhood.

2.5 Photon extraction algorithm based on local distance statistics

2.5.1 Calculation of local distance statistics

In this paper, the local sparsity rate is used to represent the photon density around the to-be-detected point. When different to-be-detected points fall into the same number of photons in the corresponding elliptical neighborhood, the distance from the to-be-detected point p to the other object points needs to be taken into account when calculating the local sparsity rate (lsr).

$$lsr_k(p) = \frac{N_{D_k(p)}}{\sum_{q \in D_k(p)} dist(p,q)}$$
(12)

 $N_{Dk(p)}$ is the number of photon points in the search elliptic neighborhood of the photon point p to be detected, and $\sum_{q \in D_k(p)} dist(p,q)$ is the sum of the elliptic distances from the point to be measured to the photon points in its elliptic neighborhood. (18)

After calculating *lsr* of each photon point, a parameter considering *lsr* of all photon points within the data segment is constructed using the mean sparse rate (*msr*) of photon points; when the current photon's *lsr* is less than the *msr*, it is discarded as a discrete noise point; conversely, when the photon's *lsr* is greater than the *msr*, the photon is placed into the signal photon candidate set for the subsequent computation process.

$$msr = \frac{\sum N_{D_k(p)}}{\sum \sum_{q \in D_k(p)} dist(p,q)}$$
(13)

 $\Sigma N_{Dk(p)}$ is the sum of the numbers of photon points within each search elliptic neighborhood of all the photon points p to be detected within the segmented dataset, and the corresponding $\Sigma \sum_{q \in D_k(p)} dist(p,q)$ is the sum of the total elliptic distances from all the photon points to be detected to the photon points within their corresponding elliptic neighborhoods.

The local distance difference coefficient (LDDC) of the current point to be detected is calculated to determine whether it belongs to the same type of photon as the surrounding points. Specifically, the LDDC measures the degree of density difference between the point under inspection and other photon points within the elliptical neighborhood. A larger LDDC indicates a higher probability that the point does not belong to the same type of photon. The specific calculation formula is as follows.

$$LDDC_{k}(p) = \frac{\sum_{q \in D_{k}(p)} lsr_{k}(q)}{N_{D_{k}(p)}} \frac{1}{lsr_{k}(p)}$$

$$(14)$$

 $\frac{\sum_{q \in D_k(p)} lsr_k(q)}{N_{D_k(p)}} \text{ is defined as the ratio of the sum of elliptical distances } lsr \text{ from the photon}$ point p (to be detected within a segmented dataset) to all photon points within its elliptical neighborhood to the total number of photon points in that neighborhood. In other words, $\frac{\sum_{q \in D_k(p)} lsr_k(q)}{N_{D_k(p)}} \text{ represents the average elliptical distance of the photon points within the neighborhood of the point under inspection. By dividing this average elliptical distance by the <math>lsr$ of the current photon point, a unique value, $LDDC_k(p)$, is obtained for each photon point to be detected.

2.5.2 Determining the segmentation threshold and removing discrete noise

Because of the different forms of spatial distribution of signal and noise photons, noise photons are discretely distributed around signal photons, and the spatial distribution of signal photons will be more concentrated than that of noise photons.⁽²¹⁾ The difference between the

current point to be measured and the neighboring photons is characterized by the local distance difference coefficient and used as a label value for each photon to be detected in the dataset to classify the noise and signal photons. If the photons to be detected and the signal photons in the neighborhood are more closely distributed and have high similarity to each other, the smaller the local distance variance coefficient is, the easier it is to be classified as a signal photon; if vice versa, the easier it is to be classified as a noise photon. OTSU is a classical threshold segmentation method usually applied to gray-scale image segmentation in image processing. (22) When dealing with photon data, the core idea is to determine the optimal threshold for distinguishing noise photons from signal photons by maximizing the interclass variance dynamics as a basis for classification. First, the histogram is calculated using the eigenvalues of the photons to estimate their probability distribution. Then, a certain threshold *T* is assumed in order to classify the photons into two categories, noise photons and signal photons, and the weights, means, and interclass variances of the two categories are calculated to find the threshold that maximizes the interclass variance. Finally, the photons with LDDC less than the threshold are classified as signal photons and those with LDDC larger than the threshold are noise photons.

2.6 Precision evaluation method

Signal photons were extracted from the ATL03 dataset using the proposed SAEN-D algorithm. To rigorously evaluate the algorithm's accuracy, manually annotated photon data served as reference data. Both quantitative metrics and qualitative analysis were employed to assess the denoising performance of the algorithm.⁽²³⁾

For quantitative evaluation, three accuracy assessment metrics were introduced: Precision (P), Recall (R), and the F1-score (F), which is the harmonic mean of Precision and Recall. The calculation formulas for these metrics are

$$\begin{cases} P = \frac{TP}{TP + FP} \\ R = \frac{TP}{TP + FN}, \\ F = \frac{2 \cdot P \cdot R}{P + R} \end{cases}$$
(15)

where TP denotes a real signal photon that was correctly detected, FP denotes a noise photon that was incorrectly classified as a signal photon, and FN denotes a real signal photon that was incorrectly detected. F is the reconciled mean of Recall and Precision, which combines the strengths and weaknesses of Recall and Precision.

For qualitative evaluation, manually annotated data were used as reference. By enlarging local details, we further compared the performance of the proposed denoising algorithm in detecting the continuity of ground photon points under complex terrain conditions.

3. Experimental Results and Analysis

3.1 Data preprocessing and preliminary noise removal

In this study, during the preprocessing of the photon dataset, the histogram statistics method is first employed to identify the effective signal range of the photons. In the two regions with differing photon elevation changes, the vertical elevation segments are divided into intervals of $\Delta h_1 = 0.5$ m and $\Delta h_2 = 25$ m. The number of photons falling within each segment is then counted. The effective signal range is extracted using the average photon count of each segment as the boundary threshold. The specific results are shown in Fig. 4, where the red photon points represent the effective signal range. In Fig. 4, it can be observed that noise photons that are clearly distant from the signal are eliminated, the photon distribution in denser regions is

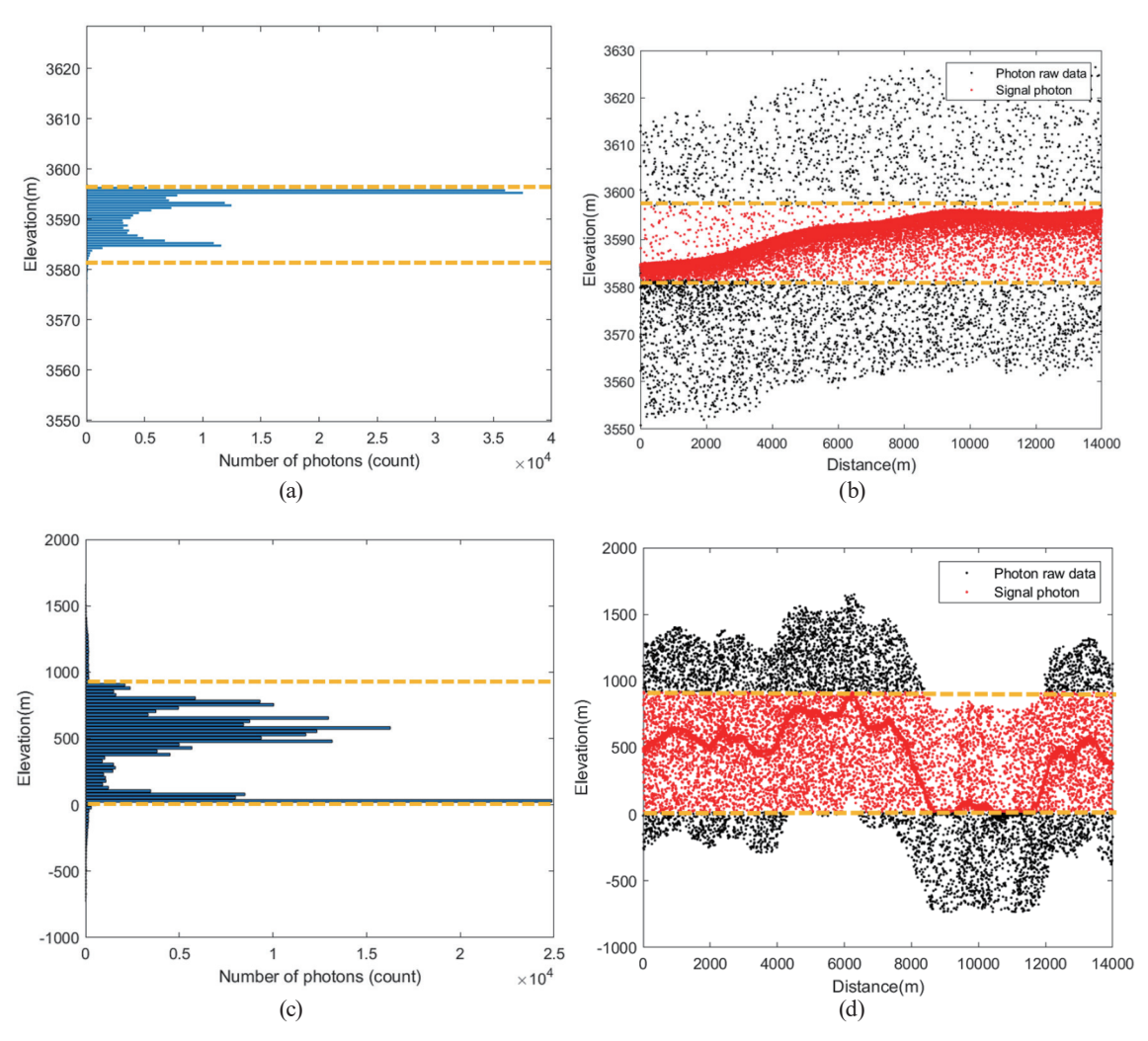


Fig. 4. (Color online) (a) and (c) Histograms of photon number elevation distribution. (b) and (d) Effective signal ranges of the intercepted photons.

retained, unnecessary computational processes are eliminated, and the foundation for the subsequent preliminary photon denoising step based on grid statistics is laid.

Next, after completing the above process, the preliminary denoising of the photons is performed using a grid-based statistical method. For two datasets with completely different terrain variations, grids of different sizes are constructed. In the relatively flat terrain of the Antarctic ice sheet, grids are constructed with a horizontal interval of $\Delta l = 50$ m and a vertical interval of $\Delta h_1 = 0.5$ m. In the rugged terrain of Greenland's ice sheet, grids are constructed with a horizontal interval of $\Delta l = 50$ m and a vertical interval of $\Delta h_2 = 25$ m. The preliminary denoising results are shown in Figs. 5(a) and 5(c). After this process, photon data with approximately 88.82% of noise removed are obtained, and the retained data align with the corresponding terrain trends. To further analyze the preliminary denoising results, the data in the along-track distance of 5000–7000 m for both datasets are focused on, as shown in Figs. 5(b) and 5(d). The blue boxes represent the grid areas of the retained data. It can be observed that, although some noise photons still remain around the signal in the retained data, there are

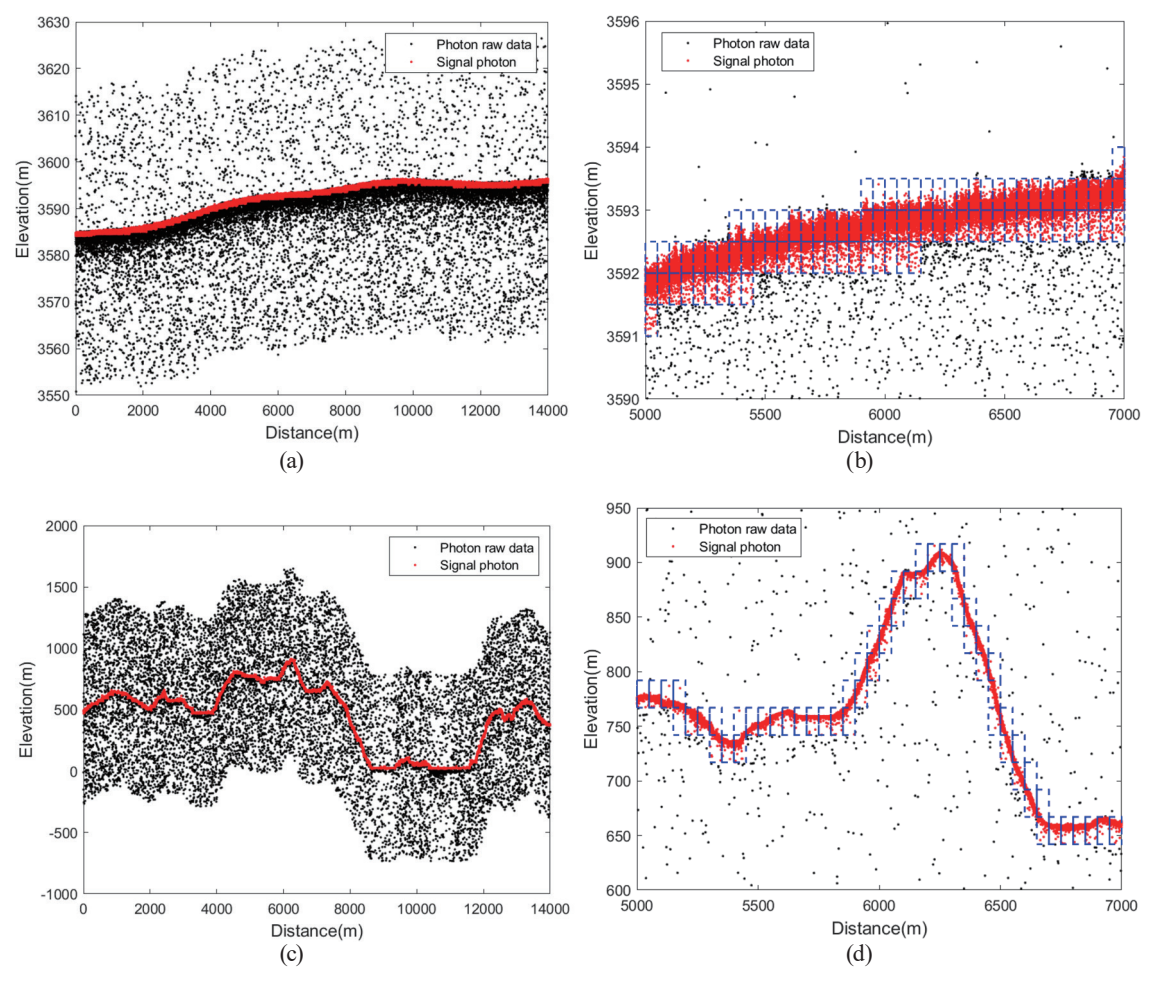


Fig. 5. (Color online) (a) and (c) Preliminary denoising results of photons based on grid statistics. (b) and (d) Enlargement of local areas of the corresponding data at along-track distances of 5000–7000 m.

significantly more noise photons below the ice sheet surface than above it, with no clear boundary between the signal photons and the noise photons.

3.2 Complex terrain adaptation analysis

3.2.1 Merging of data segments considering local topographic features

The preprocessed data are segmented in accordance with the interval of the data, the photon data falling into the segments are counted, the maximum density photon points within each segment and the slope angle of the adjacent segment datasets are found, and the terrain trend curve is fitted in accordance with the maximum density points to determine the segmentation point of the large segments. Then, the datasets with similar slope angles are merged into large segments, as shown in Fig. 6, and the processed data are shown in Figs. 6(b) and 6(d). The terrain data with similar slopes are merged into the large segments of data, which is more obvious in Fig. 6(d) where the dataset of the terrain region that rapidly descends along the track distance of

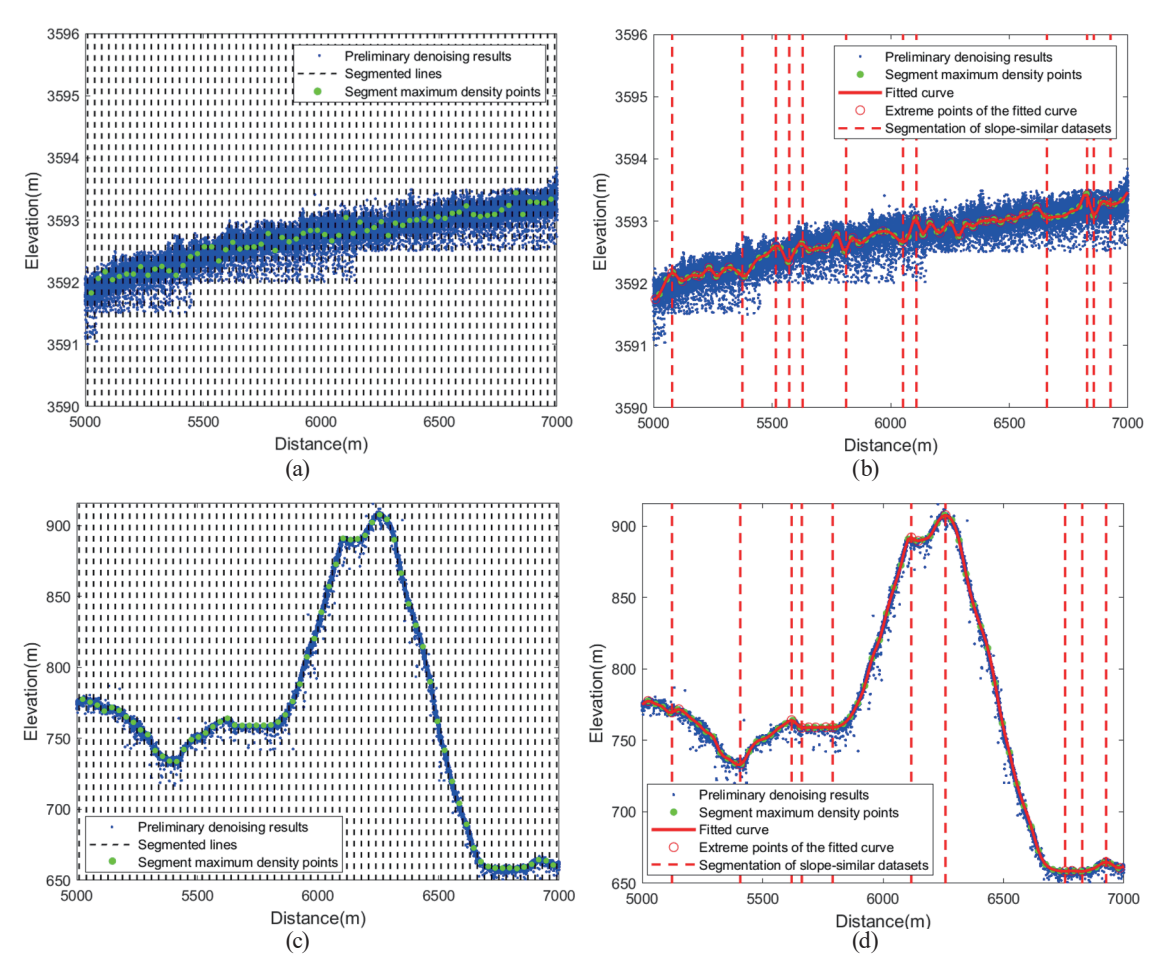


Fig. 6. (Color online) (a) and (c) Results of equidistant segmentation of DATA_1 and DATA_2 data in the region of 5000–7000 m distance along the track. (b) and (d) Results of segmentation after merging the datasets with similar slope angles.

about 6250-6750 m is merged into the same large segment of the slope dataset. At the same time, the maximum and minimum values of the slope angle dataset of the data segment are counted, which limits the slope angle of the photon data of the region to that range.

Figure 7 shows the results for the DATA_1 dataset in the along-track distance range of 4500–4800 m, with and without considering the slope reference range during photon extraction. In Fig. 7(a), when determining the elliptical neighborhood orientation of the point to be tested, photons close to the signal photons always result in the incorrect maximum density direction being calculated. This incorrect maximum density direction leads to the misidentification of these photons, as the direction of the maximum density is always towards the signal photons, as shown by the blue ellipse in Fig. 7(a). We use the slope range of the large segment of the dataset in which the photon is located to provide a reference for the calculation of the photon's θ angle, thereby distinguishing the near-surface noise photons shown in the figure. The final result after processing with the proposed algorithm is shown by the blue ellipse in Fig. 7(b). The correct maximum density direction of the elliptical neighborhood is identified, the near-surface noise photons are effectively removed, and the interference caused by anomalous ground-level signal photons is avoided, thus improving the accuracy of signal photon extraction to some extent.

3.2.2 Retention of minor terrain features

The ICESat-2 data obtained through photon-counting LiDAR is affected by the terrain, causing the distribution of signal photons to be stretched along the slope direction, while background noise photons are randomly distributed. Additionally, factors such as laser footprint energy distribution, terrain reflectivity, and cloud cover can cause significant variations in signal photon density across different regions. In flat areas, a fixed elliptical neighborhood method may perform well, but its effectiveness tends to decrease significantly in regions with steep terrain variations, such as mountainous or glacial areas. To dynamically adjust the direction and size on the basis of terrain features, ensure stable extraction performance in regions with different slopes and point cloud densities, and improve the robustness of the algorithm, we have

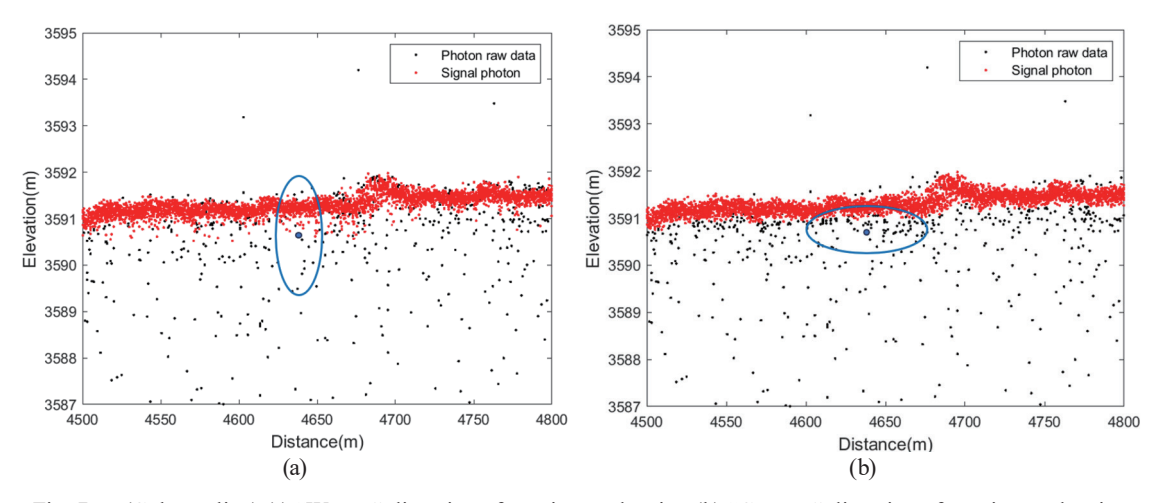


Fig. 7. (Color online) (a) "Wrong" direction of maximum density. (b) "Correct" direction of maximum density.

constructed a direction- and size-adaptive elliptical neighborhood that accounts for local terrain features in signal photon extraction. The adaptive changes in the direction and size of the elliptical neighborhood are shown in Fig. 8, where the elliptical curve in Fig. 8(b) represents the search elliptical neighborhood for the point under inspection.

The traditional fixed-size and fixed-direction elliptical neighborhood search window cannot adapt to varying terrain slopes, while the adaptive elliptical neighborhood can adjust the major axis direction on the basis of the slope direction, making the search range more reasonable. For example, in the steep slope area of the DATA_2 dataset shown in Fig. 9(a), the significant variation in terrain slope leads to regions with different photon densities in the dataset. Since the elliptical neighborhood search window is fixed horizontally and its size remains unchanged, photon extraction is less effective in the low-density photon regions. In contrast, in Fig. 9(b), the major axis of the ellipse is aligned with the slope direction, more effectively capturing the signal

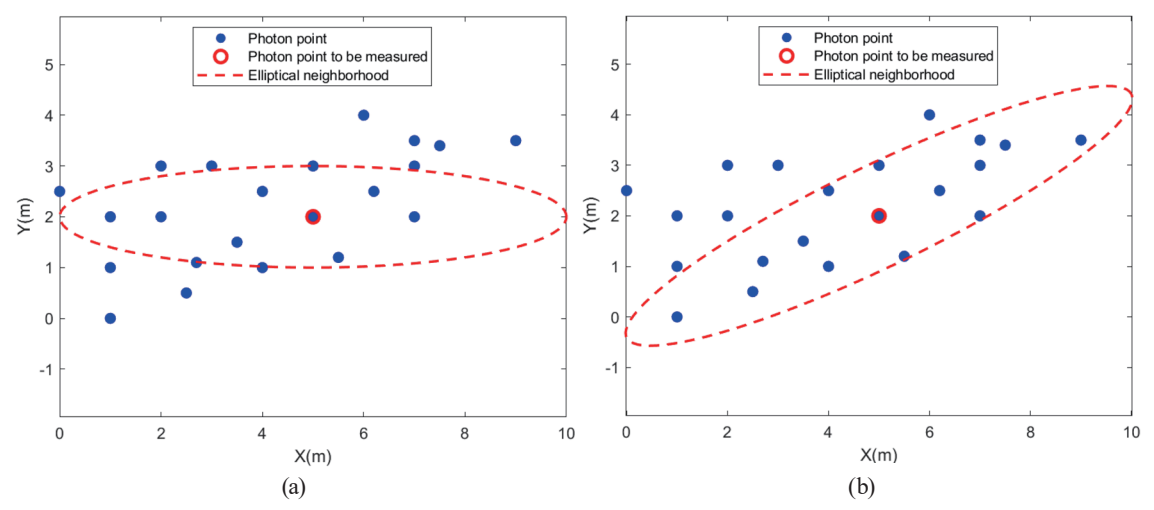


Fig. 8. (Color online) (a) Schematic of the initial horizontal elliptic neighborhood. (b) Schematic of the elliptic neighborhood direction and size adaptation.

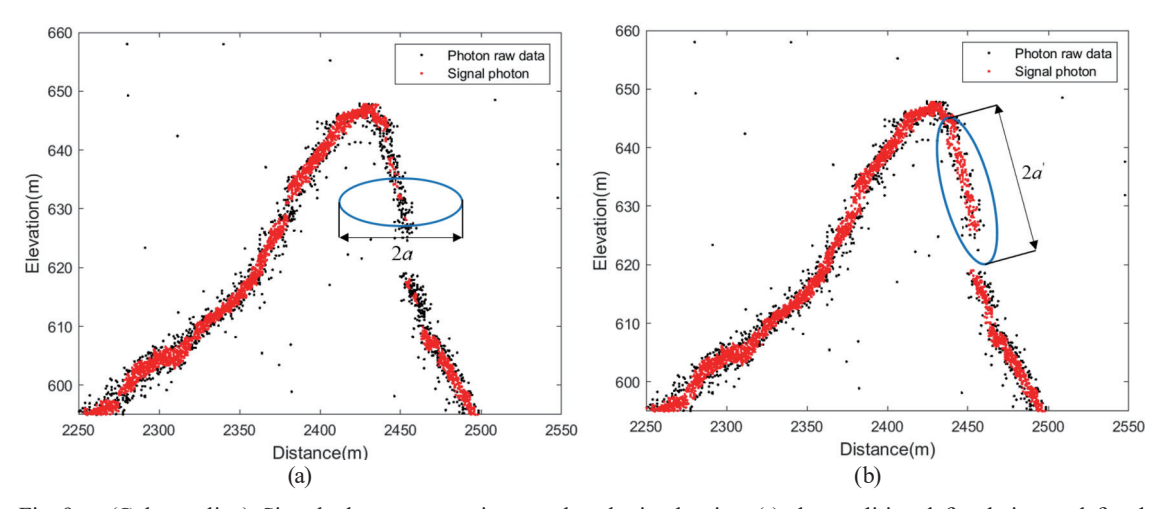


Fig. 9. (Color online) Signal photon extraction results obtained using (a) the traditional fixed-size and fixed-direction elliptical neighborhood search window and (b) the proposed SAEN-D algorithm.

photons distributed along the slope, while reducing background noise misclassification. This ensures the continuity of signal photon data in steep slope areas and improves the accuracy and stability of signal photon extraction.

3.3 Final photon extraction results and analysis

After the initial denoising, the retained photon data were segmented to form multiple datasets. For each photon within a segment, a direction- and size-adaptive elliptical neighborhood was constructed on the basis of local terrain features. Subsequently, local distance statistics were computed to extract surface signal photons. As shown in Fig. 10, noise photons near the surface were effectively removed, and the red points represent the final extracted signal photons.

For further analysis, typical regions of the two study areas in Fig. 10 are selected for detailed examination. The two regions selected in the Antarctic region are enclosed within yellow boxes marked (a) and (b), and the four regions selected in the Greenland region are enclosed within blue boxes marked (a)–(d), as shown in Figs. 11(a) and 11(b), and their corresponding specific results are shown in Figs. 12 and 13.

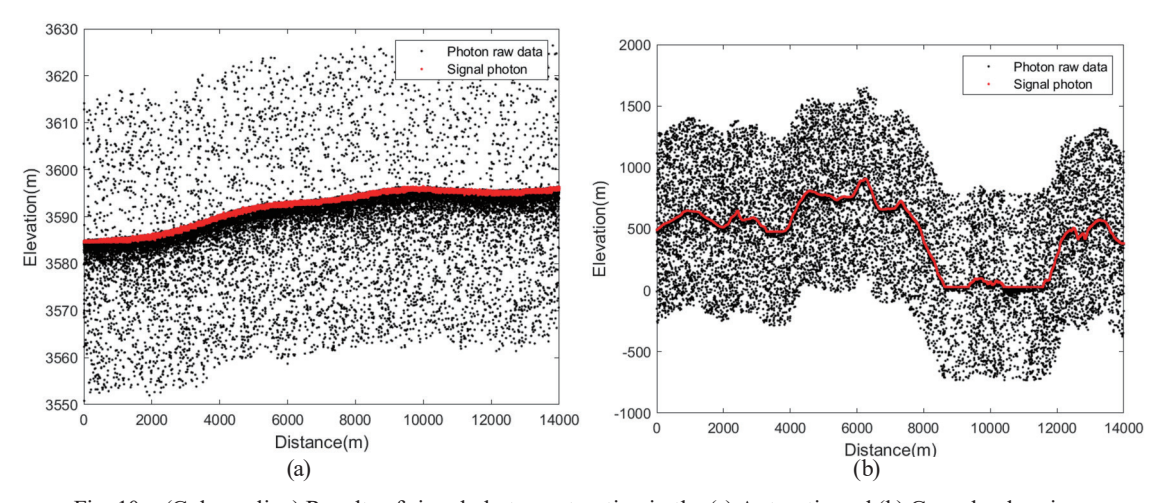


Fig. 10. (Color online) Results of signal photon extraction in the (a) Antarctic and (b) Greenland regions.

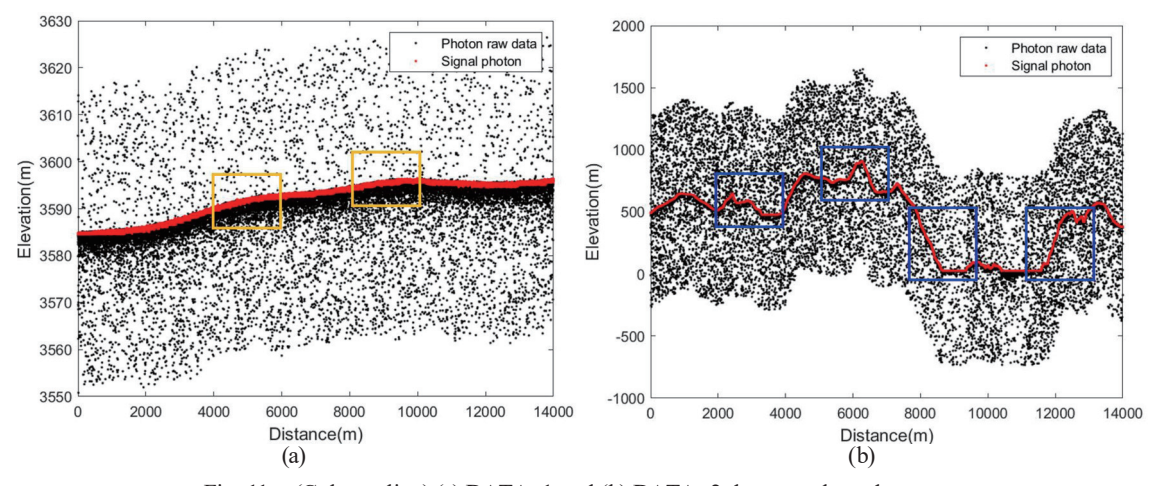


Fig. 11. (Color online) (a) DATA_1 and (b) DATA_2 dataset selected ranges.

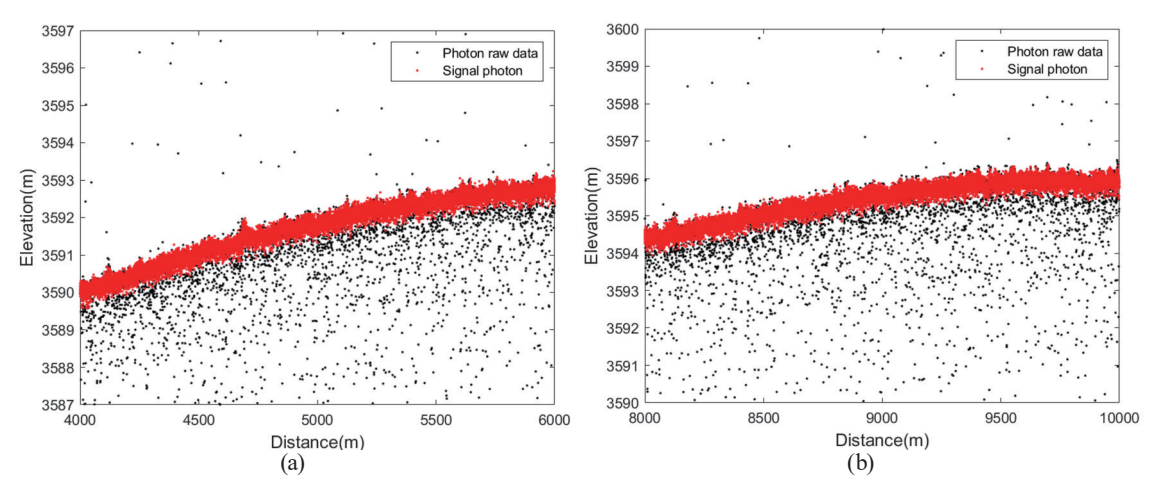


Fig. 12. (Color online) Selected photon extraction results for the DATA_1 dataset in the along-track distance ranges of (a) 4000–6000 m and (b) 8000–10000 m.

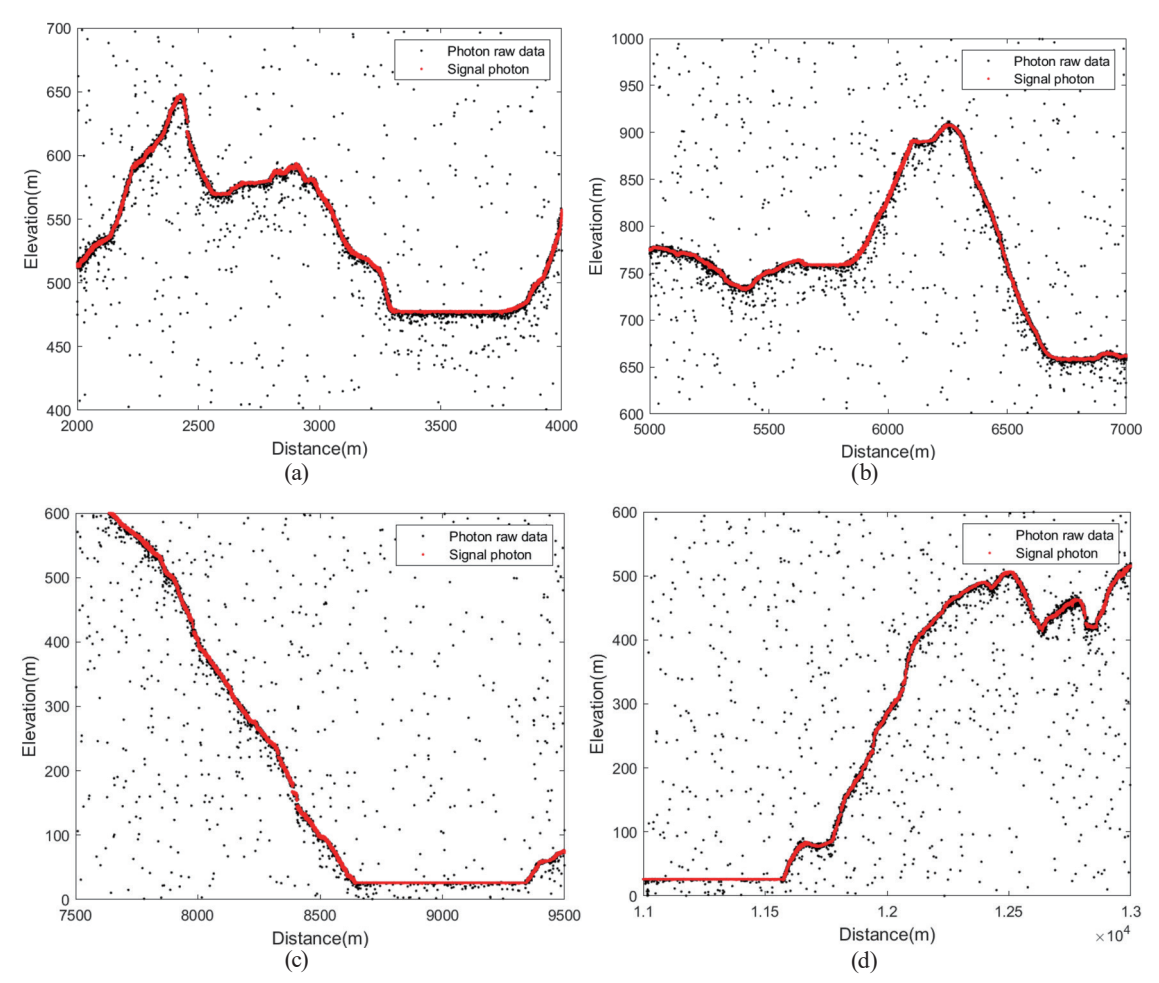


Fig. 13. (Color online) Selected photon extraction results for the DATA_2 dataset in the along-track distance ranges of (a) 2000–4000 m, (b) 5000–7000 m, (c) 7500–9500 m, and (d) 11000–13000 m.

The Antarctic ice sheet exhibits relatively flat terrain. Within two along-track intervals, the elevation fluctuations of the signal photons range between 3 and 4 m, and the signal-to-noise

ratio remains fairly uniform across different regions. In contrast, the terrain of Greenland's ice sheet varies significantly. We extract photon results from two peak positions, where the elevation fluctuation is between 200 and 300 m. Additionally, photon extraction results from regions with rapid elevation changes—both steep declines and steep rises within short distances—are also considered, with elevation fluctuations between 500 and 600 m. Because of the complex terrain, the signal-to-noise ratio differs across regions, and in some areas, the surface photon density is sparse, leading to elevation gaps. For the elevation gap regions in Greenland, the proposed method can detect as many signal photons as possible while maintaining accuracy. Overall, the proposed method has demonstrated good performance in six different terrain regions, including flat terrain, terrain inflection points, and areas with steep elevation changes. It effectively removes noise photons while ensuring the continuity of signal photon data and can retain minor terrain features, which would otherwise be ignored as discrete noise.

3.4 Accuracy validation

To assess the accuracy of the denoising algorithm proposed in this paper on the basis of the neighborhood ellipse direction and size adaptive change of local distance statistics, manually visually labeled photon data are used as the validation data, and three accuracy evaluation indexes P, R, and F are introduced to quantitatively assess the denoising effect of the algorithm. Two datasets with a total of six regions are selected for accuracy verification, and the specific results are shown in Table 1. The ILSC algorithm, (18) which maintains a horizontal direction and fixed size for the search elliptical neighborhood, is compared with the proposed photon denoising algorithm in terms of the local terrain-feature-based adaptive direction and size of elliptical neighborhoods. In the relatively flat terrain of the Antarctic region (a), the F values for the ILSC algorithm and the proposed method are 95.22 and 98.14%, respectively. For the region (b) data, the F values for the ILSC algorithm and the proposed method are 95.15 and 97.07%, respectively. Both denoising algorithms achieved good results, demonstrating the effectiveness of the two methods. For the data from the four regions of Greenland with rugged terrain, the F values for

Table 1 Accuracy evaluation results of two denoising algorithms.

Detect	Region	Algorithm -	Metric parameters (%)		
Dataset			P	R	\overline{F}
DATA_1 (Gentle slopes)	(a)	ILSC	97.09	93.41	95.22
		SAEN-D	98.13	98.15	98.14
	(b)	ILSC	93.93	96.40	95.15
		SAEN-D	96.54	97.61	97.07
DATA_2 (Steep slopes)	(a)	ILSC	93.65	90.22	91.90
		SAEN-D	99.97	94.69	97.26
	(b)	ILSC	92.00	92.62	92.31
		SAEN-D	99.12	97.38	98.24
	(c)	ILSC	89.56	87.60	88.57
		SAEN-D	99.60	96.94	98.25
	(d)	ILSC	90.25	87.60	88.91
		SAEN-D	99.76	92.75	96.13

the ILSC algorithm are 91.90, 92.21, 88.57, and 88.91%. In contrast, the *F* values for the proposed method reach 97.26, 98.24, 98.25, and 96.13%, representing an improvement of 7.8% over the traditional ILSC algorithm. Under the same denoising parameter conditions, the ILSC algorithm fixes the search elliptical neighborhood in the horizontal direction. When the terrain changes, the number of photons in the horizontal direction significantly decreases, causing photons that should be identified as signals to be misclassified as noise. In contrast, the proposed algorithm adapts to the local terrain features, dynamically adjusting the direction and size of the elliptical neighborhood, overcoming the challenge of discontinuous signal extraction caused by uneven photon distribution in both horizontal and vertical directions. Furthermore, the ILSC algorithm performs reasonably well on the relatively flat terrain of Antarctica, which further supports the above inference.

At the same time, we also visually compare the results obtained by the ILSC algorithm and the proposed algorithm. Taking the Greenland region (with complex terrain) as an example, the specific results are shown in Fig. 14. Figures 14(a)–14(d) show the results obtained by the proposed algorithm in the Greenland region, while Figs. 14(e)–14(h) show the results obtained by the ILSC algorithm (where the search elliptical neighborhood maintains at a horizontal direction with a fixed size).

In our proposed method, the direction of the elliptical neighborhood is adaptively aligned with the local slope, and its size is dynamically adjusted by modifying the semi-major axis in accordance with local topographic features. This allows for more accurate density estimation on inclined surfaces across different regions. The ILSC algorithm, originally designed for shallow marine areas with relatively flat terrain, demonstrates good robustness in such environments. However, when applied to areas with significant topographic variation, it does not adapt the direction and size of the elliptical search neighborhood on the basis of local terrain changes. As a result, although it can retain some signal photons in flat regions, signal photons in rugged areas are often misclassified as noise and are removed. This leads to discontinuities in the signal photon distribution over the ice cap surface and the poor preservation of subtle topographic undulations.

By comparing the two methods, it can be concluded that the ILSC algorithm is more suitable for data processing in relatively flat areas, but is not effective in regions with significant topographic variations, whereas the algorithm proposed in this paper demonstrates clear advantages in rugged terrain.

4. Discussion

4.1 Methodological innovation and theoretical contribution

The SAEN-D algorithm proposed in this paper effectively adapts to anisotropic photon distributions and enhances the accuracy of signal extraction in photon data processing over complex terrains. Compared with existing methods, its innovations are highlighted in the following two aspects:

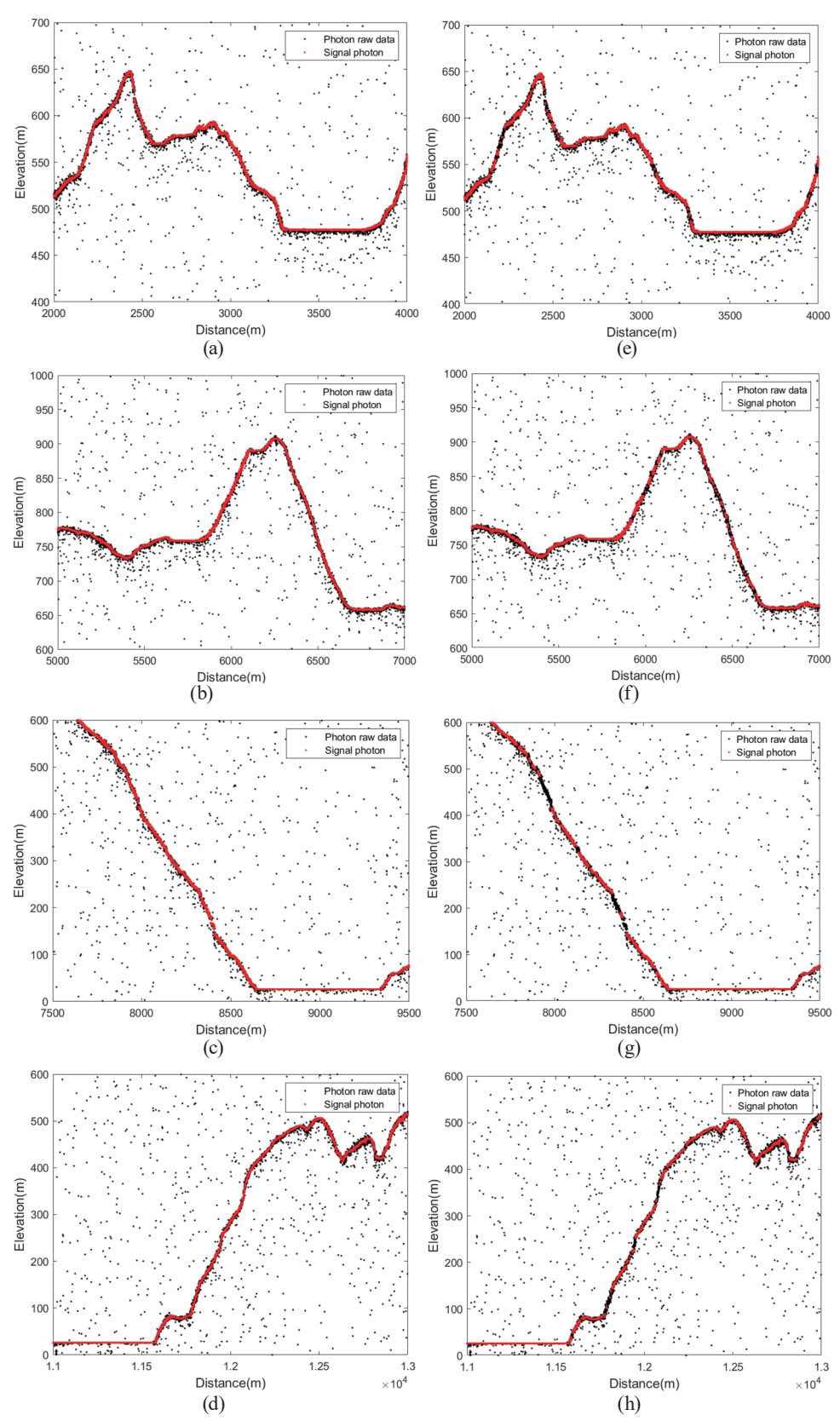


Fig. 14. (Color online) (a)—(d) Results of the proposed method in typical regions of Greenland. (e)—(h) Results of the ILSC algorithm in the same typical regions.

Dynamic segmentation and merging strategy: By adopting the segmentation method of cubic spline interpolation and curvature detection, the equidistant along-track data are segmented and merged by considering the local topographic features, and the merged dataset and the slope angle dataset are constructed, providing a slope reference for the determination of the direction of the subsequent search ellipse.

Direction-slope dynamic coupling mechanism: Correlating the ellipse direction with the local slope angle solves the signal leakage detection problem of traditional fixed-direction ellipses (e.g., ILSC algorithm) in steep slope regions. The results of experiments show that our method improves the signal extraction accuracy by 7.8% in the steep-slope region of Greenland, which verifies the adaptability of the direction adaptation to the anisotropy of photon distribution.

The results of this study demonstrate that the direction- and scale-adaptive mechanism combined with segment merging effectively addresses photon distribution anisotropy in complex terrain, reduces signal leakage and misclassification, and improves the quality of ATL03 data products. This provides a solid foundation for high-precision elevation inversion and the dynamic monitoring of ICESat-2 data while also offering valuable insights for optimizing next-generation LiDAR systems. The two study areas in this investigation are both ice-sheet-covered regions. Utilizing high-precision surface-elevation-change data from these ice sheets enables us to infer the ice mass balance and assess their contribution to global sea-level rise, which is critical for polar environmental research and the early warning of disaster. Furthermore, ice sheet regions represent some of the most challenging environments for remote sensing algorithm validation. The proposed algorithm can be extended to other heterogeneous terrains, such as mountain glaciers, snow-covered areas, and permafrost zones, thereby contributing to the advancement of a global high-precision terrain change monitoring system.

4.2 Limitations and insights

Although the proposed denoising algorithm demonstrates good adaptability and robustness in complex terrain environments, significantly improving the accuracy of photon signal extraction, it still has certain limitations. On one hand, the algorithm faces a risk of misidentifying isolated signals under extremely low signal-to-noise ratio conditions, revealing a potential stability bottleneck. On the other hand, the method shows sensitivity to key parameters, such as grid window size and segmentation threshold scaling factors, and partially depends on the prior specification of regional features, which limits its systematic applicability and reproducibility across different datasets.

The aforementioned issues offer valuable directions for future research. First, integrating multisource data—such as ICESat-2 trajectory data with imagery, digital elevation models (DEMs), and InSAR—can enable spatial feature-assisted discrimination, thereby enhancing the algorithm's generalization capability. Second, exploring intelligent denoising approaches based on deep learning or graph neural networks can reduce the reliance on empirically defined parameters, improving processing efficiency and adaptability. By continuously optimizing the algorithm architecture and incorporating more diverse information sources, the accuracy and automation level of photon data processing in ice cap regions can be further improved, providing

more reliable data support for polar environmental monitoring and ice sheet dynamic analysis.

Moreover, the stability demonstrated by the denoising algorithm in complex regions suggests its generalizability and potential applicability to other environments—particularly those characterized by significant topographic variability or marked changes in photon density, such as coastal and forested areas. However, in practical applications, the construction of the elliptical neighborhood may require fine-tuning to make it adaptable to specific environments and ensure robust performance across diverse scenarios. In coastal regions, the photon point cloud density is affected by factors such as water transparency and depth. In certain underwater areas, photon data may be sparse or missing altogether. Therefore, parameters such as water depth and transparency should be incorporated into the elliptical neighborhood construction. In forested regions, terrain is often highly complex, and photon density may exhibit significant fluctuations, especially beneath the canopy, where signals are uneven owing to vegetation occlusion. In such cases, integrating forest structural information (e.g., canopy height and tree species) and constructing refined models of photon density distribution can help optimize the size and orientation of the elliptical neighborhood, thereby improving the algorithm's adaptability to environmentally complex regions.

5. Conclusions

The SAEN-D algorithm proposed in this paper for ICESat-2 data can adaptively adjust the direction of the elliptical major axis to align with the local slope, while changing the semimajor axis in accordance with local topographic features to control the size of the elliptical neighborhood. This approach enables the construction of the optimal search elliptical neighborhood to calculate elliptical density, achieving a denoising effectiveness with an F value greater than 95% across various terrain regions. The algorithm overcomes, to some extent, the impact of complex terrain undulations and uneven photon density distribution, addressing the limitations of fixed-threshold denoising algorithms. It is capable of removing noise photons while ensuring the continuity of signal photons, and it demonstrates relatively stable performance in areas with slope changes, showing good robustness. In particular, in the Greenland region, the signal extraction accuracy improved by 7.8%, verifying the effectiveness of the algorithm.

Further research will show that the combination of the direction- and scale-adaptive mechanism with the segment merging strategy effectively addresses the issue of photon distribution anisotropy in complex terrains, reduces signal omission and misjudgment, and improves the quality of ATL03 data products. This provides a solid foundation for high-precision elevation inversion and dynamic change monitoring using ICESat-2 data. On the other hand, for regions with complex surface cover types—such as forested areas and nearshore shallow reefs with varying water qualities and low signal-to-noise ratio environments—the adaptability of the algorithm still requires further optimization. Future research will focus on extending the applicability of the proposed method to a wider range of surface feature types, aiming to meet the demands of high-precision global terrain change monitoring and to provide a solid technical foundation for the development of advanced sensor technologies and terrain monitoring systems.

Acknowledgments

We would like to thank NSIDC (https://doi.org/10.5067/ATLAS/ATL03.005) for providing the ICESat-2 ATL03 product. We also acknowledge the funding from the National Natural Science Foundation of China (No. 42371441).

References

- 1 H. Xie, D. Ye, Q. Xu, Y. Sun, P. Huang, X. Tong, Y. Guo, X. Liu, and S. Liu: IEEE Trans. Geosci. Remote Sens. **60** (2022) 1. https://doi.org/10.1109/TGRS.2022.3176982
- 2 L. Magruder, T. Neumann, and N. Kurtz: Earth Space Sci. 8 (2021) 25. https://doi.org/10.1029/2020EA001555
- 3 X. X. Zhu, S. Nie, C. Wang, X. H. Xi, J. S. Wang, D. Li and H. Y. Zhou: IEEE Geosci. Remote Sens. Lett. 18 (2021) 1471. https://doi.org/10.1109/LGRS.2020.3003191
- 4 X. X. Zhu, C. Wang, X. H. Xi, S. Nie, X. B. Yang, and D. Li: Infrared Laser Eng. **49** (2020) 20200259 (in Chinese). http://dx.doi.org/10.3788/IRLA20200259
- 5 Y. J. Li, X. Q. Zhou, G. Y. Li, J. Q. Guo, Y. Ma, and Y. F. Chen: Infrared Laser Eng. **51** (2022) 10 (in Chinese). http://dx.doi.org/10.3788/IRLA20220003
- 6 H. Xie, Q. Xu, D. Ye, J. Jia, Y. Sun, P. Huang, M. Li, S. Liu, F. Xie, X. Hao, and X. Tong: IEEE J. Sel. Top. Appl. Earth Obs. Remote Sens. 14 (2021) 7604. https://doi.org/10.1109/JSTARS.2021.3094195
- 7 D. Wang, J. Yu, F. Liu, and Q. Li: Earth Planets Space. **76** (2024) 128. https://doi.org/10.1186/s40623-024-02071-y
- 8 J. Li, W. J. Meng, J. Y. Hao, Z. P. Dong, and Q. H. Tang: Coast. Eng. **43** (2024) 263 (in Chinese). http://dx.doi.org/10.12362/j.issn.1002-3682.20240620001
- 9 X. D. Li, Z. M. Gao, X. D. Chen, S. F. Sun, and J. Q. Liu: Information 12 (2021) 235. https://doi.org/10.3390/info12060235
- 10 L. Magruder, W. Iii, K. Stout, and A. Neuenschwander: Proc. SPIE Int. Soc. Opt. Eng. 8379 (2012) 24. http://dx.doi.org/10.1117/12.919139
- B. W. Chen and Y. Pang: Proc. SPIE 9671, AOPC 2015: Advances in Laser Technology and Applications (2015) 96711S. https://doi.org/10.1117/12.2202777
- 12 M. S. Awadallah, S. Ghannam, L. Abbott, and A. M. Ghanem: 13th Int. Conf. LiDAR Applications for Assessing Forest Ecosystems (2013) 129.
- 13 J. Zhang and J. Kerekes: IEEE Geosci. Remote Sens. Lett. **12** (2015) 726. https://doi.org/10.1109/LGRS.2014.2360367
- 14 Y. Ma, W. H. Zhang, J. Y. Sun, G. Y. Li, X. H. Wang, S. Li, and N. Xu: Remote Sens. 11 (2019) 471. https://doi.org/10.3390/rs11040471
- 15 A. Neuenschwander and K. Pitts: Remote Sens. Environ. 221 (2019) 247. https://doi.org/10.1016/j.rse.2018.11.005
- 16 U. Herzfeld, T. Trantow, D. Harding, and P. Dabney: IEEE Trans. Geosci. Remote Sens. PP (2017) 1. https://doi.org/10.1109/TGRS.2016.2617323
- B. Chen, Y. Pang, Z. Li, H. Lu, L. Liu, P. R. J. North, and J. A. B. Rosette: IEEE Geosci. Remote Sens. Lett. 16 (2019) 1447. https://doi.org/10.1109/LGRS.2019.2899011
- 18 K. F. Luan, K. N. Zhang, Z. G. Qiu, J. Wang, Z. H. Wang, Y. Xue, W. D. Zhu, D. D. Lin, and X. Y. Zhao: Natl. Remote Sens. Bull. 27 (2023) 520 (in Chinese). https://dx.doi.org/10.11834/jrs.20221854
- 19 G. H. He, H. Wang, Q. Fang, Y. A. Zhang, D. L. Zhao, and Y. P. Zhang: J. Infrared Millim. 42 (2023) 250 (in Chinese). http://dx.doi.org/10.11972/j.issn.1001-9014.2023.02.016
- 20 F. Xie, G. Yang, R. Shu, and M. Li: J. Infrared Millim. 36 (2017) 107 (in Chinese). http://dx.doi.org/10.11972/j.issn.1001-9014.2017.01.019
- L. Y. Gu, D. Z. Fan, S. Ji, Z. H. Gong, D. Z. Li, and Y. Dong: Sensors 23 (2023). https://doi.org/10.3390/s23218752
- 22 N. Otsu: IEEE Trans. Syst. Man Cybern. 9 (1979) 62. https://doi.org/10.1109/TSMC.1979.4310076
- 23 Q. Xu, H. Xie, Y. Sun, X. Liu, Y. Guo, P. Huang, B. Li, and X. Tong: Int. Arch. Photogramm. Remote Sens. Spatial Inf. Sci. XLIII-B2-2022 (2022) 309. https://doi.org/10.5194/isprs-archives-XLIII-B2-2022-309-2022

About the Authors



Kuifeng Luan received his Ph.D. degree in cartography and geographical information engineering from the College of Surveying and Geo-Informatics, Tongji University, in 2017. He is currently a professor at the College of Oceanography and Ecological Environment, Shanghai Ocean University. His research focuses on the intelligent mapping of marine topography and geomorphology using multisource remote sensing. His main research areas include LiDAR data processing and marine mapping, UAV-based ocean observation and remote-sensing big data processing, as well as marine geophysical observation and analysis. (kfluan@shou.edu.cn)



Lizhe Zhang received her B.S. degree from Shandong University of Science and Technology, China, in 2022. She is expected to obtain her M.S. degree from Shanghai Ocean University in 2025. Her research interests mainly include LiDAR point cloud data processing, the study of underwater laser transmission characteristics in turbid waters, as well as Matlab simulation and data analysis. (m220200695@st.shou.edu.cn)



Weidong Zhu received his Ph.D. degree in photogrammetry and remote sensing from Tongji University in 2011. He is currently an associate professor and master's supervisor at the College of Oceanography and Ecological Environment, Shanghai Ocean University. His research focuses on marine surveying and remote sensing, with key areas including active and passive bathymetric inversion, full-waveform LiDAR shallow water depth measurement, water environment remote sensing, and high-precision GNSS positioning. (wdzhu@shou.edu.cn)



Wei Kong received his Ph.D. degree in space physics from the School of Electronic Information, Wuhan University, Wuhan, China, in 2015. He is currently a research associate professor and doctoral supervisor with the Shanghai Institute of Technical Physics, Chinese Academy of Sciences, Shanghai, China. His current research interests include laser detection technology in extreme sensitivity space and applications in Earth observation. (kongwei@mail.sitp.ac.cn)



Lin Liu received her bachelor's degree from Shandong University of Science and Technology in 2022. She is currently a master's student in the 2023 cohort at Shanghai Ocean University, majoring in oceanography. Her research focuses on the application of photon LiDAR in shallow-sea seabed sediment classification. (karinliu1113@163.com)



Jinhui Zheng received her B.S. degree from Shandong University of Science and Technology in 2021. She is expected to obtain her M.S. degree from Shanghai Ocean University in 2025. Her research interests focus on the mechanism of background noise in LiDAR, the processing of airborne and spaceborne point cloud data, as well as Matlab simulation and data analysis. (zhengjh6698@163.com)



Peiyao Zhang received her B.S. degree from Shandong University of Science and Technology, China, in 2022. Since 2023, she has been pursuing her M.S. degree at Shanghai Ocean University, China. Her research interests are in the processing of single-photon LiDAR data, bathymetry, and refraction correction. (zpy6857@163.com)



Xiangrong Chen received his B.S. degree from Shanghai Ocean University in 2024. He is currently a graduate student majoring in Oceanography at Shanghai Ocean University, Class of 2024. His research focuses on photon-counting LiDAR. (Chenxr@shou.edu.cn)



Hui Jiang received her B.S. degree from Sichuan Normal University in 2024. She is currently pursuing her M.S. degree with the College of Oceanography and Ecological Science, Shanghai Ocean University. Her research interests include airborne laser bathymetry. (jianghui1112@163.com)